

Phase field crystal modelling of deformation assisted precipitation in binary alloys

Alex Mamaev,^{1,*} Duncan Burns,² and Nikolas Provatas¹

¹*Department of Physics, Centre for the Physics of Materials, McGill University, Montreal, QC, Canada H3A 2T8*

²*McCormick School of Engineering, Northwestern University, Evanston, IL, United States 60208*

(Dated: October 10, 2024)

We consider the process of precipitation in binary alloys in the presence of mechanical deformation. It is commonly observed that mechanical deformation prior to or during precipitation leads to microstructure with excess defects, which allows for enhanced precipitate nucleation and growth rates [1–3]. To investigate this phenomenon, we employ a two-dimensional phase-field crystal alloy model endowed with a temperature dependent mobility, making it capable of recovering isothermal transformation (TTT) diagrams with a characteristic inflection point (nose) about a critical temperature. We examine the variation in the time-scale of precipitation and its connection to the time-scale of the applied deformation, focusing on the roles of atomic defects in the processes involved. Our results indicate that precipitation is initially delayed through application of a deformation until a critical strain is achieved, beyond which precipitation proceeds more rapidly, assisted by plastic deformation such as grain boundary buckling or dislocation nucleation. We show that the evolution of the precipitated fraction, $f(t)$, departs from classical Avrami behaviour. Specifically, df/dt develops two peaks indicative of a “plateau”-like inflection in $f(t)$, signalling the transition to defect assisted precipitate nucleation. We analyze these plateaus as a function of the deformation rate and demonstrate that they exhibit a discontinuous bifurcation as the time-scale of applied deformation is increased. These findings are compared to and found to be consistent with experiments.

Mechanical deformations driving out-of-equilibrium behaviours are ubiquitous in current and emerging material processing techniques such as additive manufacturing, laser shock peening, friction stir-welding, etc. [4–6]. The material conditions left behind in the wake of these processes provide inflated driving forces for diffusive and phononic relaxation due to increased saturation of solid solutions and the presence of point defects. This is in sharp contrast to classical casting conditions [7, 8]. An emphasis on the physics governing the aforementioned material processes has thus been of interest to the materials science community, particularly how such processes deviate from classically understood mechanisms of precipitation, recrystallization and recovery in metal alloys.

Precipitation readily occurs at sites of higher energy, such as defects and grain boundaries. Mechanical deformation of crystalline solids produces many such sites, thus modifying the nucleation, growth, and coarsening properties encountered [3]. Precipitation can thus be seen as competitive with other forms of strain relaxation eg. recrystallization and recovery in metals and their alloys. These processes all use stored driving forces to relieve stress accruing at high energy sites within a deformed sample. Indeed, this has been studied previously [1, 2], where experiments and numerical simulations have examined modifications to isothermal transformation (TTT) diagrams in the presence of mechanical deformation. Analytical models have likewise been formulated to quantify this interactive growth process [9]. These models typically require a priori knowledge of specific material properties which are difficult to extract such as activation energies, defect fractions. Furthermore, these models require knowledge of the nucleation and growth mechanisms of both recrystallized and precipitated grains.

Recent indirect experimental measurements, such as in-situ small-angle X-ray scattering of deforming Al-Zn-Mg-Cu, have provided detailed views of the kinetics of precipitation

[3, 10]. These studies have demonstrated an enhanced precipitation, in particular, an enhanced precipitated volume fraction growth rate is observed upon application of deformation, argued to be a result of an increased defect density. Despite these advances, direct in-situ observation of microstructure evolution is typically impossible. Hence, the nano-scale mechanisms involved in the formation of precipitates cannot be thoroughly examined experimentally, and many questions about defect-assisted precipitation remain. Due to the above challenges, the development and application of numerical modelling methods to examine the nano-scale behaviour during such processes becomes crucial.

The phase-field crystal (PFC) technique is an atomistic modelling approach for microstructure evolution that, unlike traditional phase-field modelling, is capable of simulating the coupled evolution of solute diffusion and the effects of lattice orientation, grain boundaries, dislocations, and thermal and solute based strain effects on experimentally relevant length and time-scales [11–18]. Moreover, by introducing a second time-scale into the density evolution, PFC models may also support quasi-phononic relaxation while remaining orders of magnitude faster than molecular dynamics simulations [19–21]. This endows PFC models with the ability to effectively examine the interplay between recrystallization and precipitation.

In order to investigate the atomistic behaviour of precipitation in the presence of deformation, this work examines a prototypical scenario of an equal tilt bicrystal undergoing a continuous compressive deformation with strain rate $\dot{\epsilon}$. To this end, we employ a structural phase field crystal (XPFC) model with a free energy functional that models substitutional binary alloys and has previously been applied to studies involving precipitation [22, 23], as well as deformation in such

systems [24]. Our free energy is formulated as follows,

$$\frac{\Delta F}{k_B T^0 \rho^0} = \tau \int d\mathbf{r} \left\{ \frac{1}{2} n^2 - \frac{\eta}{6} n^3 + \frac{\chi}{12} n^4 + \omega \Delta F_{mix} + \frac{W_c}{2} |\nabla c|^2 - \frac{1}{2} n \int d\mathbf{r}' C_{nn}^{(2)}(|\mathbf{r} - \mathbf{r}'|) n' \right\}, \quad (1)$$

where $n = (\rho - \rho^0)/\rho^0$ measures the local coarse grained density relative to a reference density, ρ^0 corresponding to the expansion point of the model, $\tau = T/T^0$ is a dimensionless temperature and c is the local solute concentration field. Here, η and χ control deviations from the ideal gas free energy, W_c controls the diffusion length of the c field and ω controls the free energy of mixing, given by

$$\Delta F_{mix} = (1+n) \left\{ c \log\left(\frac{c}{c_0}\right) + (1-c) \log\left(\frac{1-c}{1-c_0}\right) \right\}, \quad (2)$$

where c_0 is the concentration at the reference. The final, excess, term of the free energy controls the length scale and strength of atomic-scale interactions. The correlation function C_{nn} interpolates between pure A and pure B structures through interpolation functions $\chi_A(c) = 1 - 3c^2 + 2c^3$, $\chi_B(c) = 1 - 3(1-c)^2 + 2(1-c)^3$ such that $C_{nn}(\mathbf{r} - \mathbf{r}') = \chi_A C_{AA}^{(2)}(\mathbf{r} - \mathbf{r}') + \chi_B C_{BB}^{(2)}(\mathbf{r} - \mathbf{r}')$. In XPFC, the pure species correlation functions are defined in Fourier space (with wave-vector magnitude k) by a sum of Gaussian functions centered about the dominant reciprocal lattice wave-vector ($k = k_i$) and $k = 0$ modes of each species respectively,

$$\hat{C}_{ii}^{(2)}(k) = e^{-\frac{T}{T_i^0}} \left\{ -A_0 e^{-\frac{k^2}{2\sigma_{i,0}^2}} + e^{-\frac{(k-k_i)^2}{2\sigma_{i,1}^2}} \right\}, \quad (3)$$

where $i = A, B$. The parameter T_i^0 controls the temperature scaling of the corresponding correlation function, $\sigma_{i,0}$ and $\sigma_{i,1}$ control the Gaussian widths of the $k = 0$ and dominant wave-vector respectively. Finally, $A_{i,0}$ is constant that controls the amplitude of the $k = 0$ mode. In this letter, we work in two spatial dimensions and employ a single wave-vector in our correlation to stabilize a hexagonal structure in each solid phase.

To evolve the n and c fields, we apply conserved dynamics,

$$\frac{\partial^2 n}{\partial t^2} + \beta \frac{\partial n}{\partial t} = \nabla M_n \cdot \nabla \mu_n + \xi_n, \quad (4)$$

$$\frac{\partial c}{\partial t} = \nabla M_c \cdot \nabla \mu_c + \xi_c, \quad (5)$$

where $\mu_{n/c}$ are the chemical potentials, $M_{n/c}$ are the mobilities and $\xi_{n/c}$ are noise sources applied to the n and c fields respectively. We also add an additional time-scale for quasi-phonon relaxation into the density equation. A full two-time scale model involving the couplings to c are outside of the scope of this work. The noise terms satisfy their respective fluctuation dissipation relations, $\langle \xi_{n/c}(\mathbf{r}, t) \xi_{n/c}(\mathbf{r}', t') \rangle = N_{n/c} M_{n/c} k_B T \delta(\mathbf{r} - \mathbf{r}') \delta(t - t')$ where $N_{n/c}$ subsume remaining constant prefactors and are treated as model parameters.

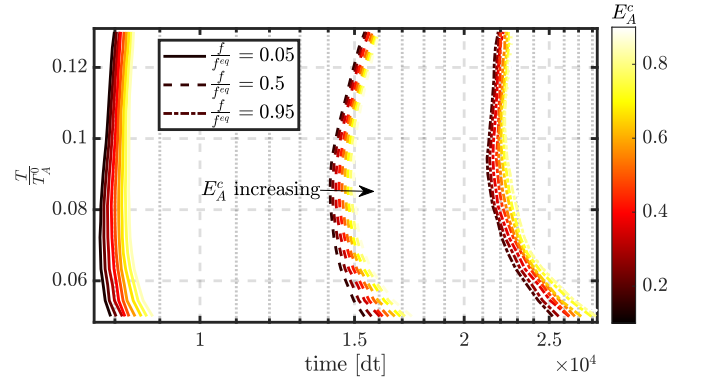


FIG. 1: The isothermal transformation (TTT) diagram of precipitation at zero strain rate. The three sets of curves represent different fractions of completed transformation. A characteristic inflection or nose shape can be observed over the range of temperatures selected as a result of the temperature dependent mobilities defined in Eq. (6). Curves are plotted for a selection of E_A^c , which monotonically controls the reaction rate as shown.

We note that these dynamics are not strictly consistent in the regime where the average density of the system has significant variations [25]. A more rigorous albeit more computationally expensive treatment of the dynamics has been implemented in [26]. However, as the common tangents between the free energy wells of our system exist at small and nearly identical average densities, this approximation is justified.

While our systems are assumed to be isothermal, We expand on the model by introducing temperature dependent mobilities into the system dynamics. As will be shown below, this allows for the generation of TTT curves that can be controlled through model parameters. An Arrhenius form is assumed for the mobilities of both n and c ,

$$M_{n/c} = M_{n/c}^0 e^{-E_A^{n/c}/k_B T} \quad (6)$$

where the activation energies E_A^n , E_A^c are model parameters which control the curvature and position of the inflection point of a given TTT curve for precipitation. Strictly speaking, these will be coupled to the mobilities of the individual atomic species in a non-linear manner. For convenience, we treat these mobilities and activation energies as independent model parameters for the purposes of this study. It is also noted that the modified mobilities will shift the effective length-scale over which quasiphonons propagate undamped for fixed values of β .

For all simulations described, we performed a quench below the solvus line into solid-solid coexistence. Full simulation parameters are presented in the Supplemental Material. We initialize the density field of the crystalline regions by seeding in an equal tilt bicrystal through a one-mode expansion. The lattice constant of this solid solution is set to be commensurate to the value attained by the interpolated correlation function for the given choice of supersaturation. The system is set to be initially strain-free by performing a minimization over the angle and number of atoms in the x and y directions for one (and by symmetry the other) grain as in [27]. The initial misorientation during this minimization was

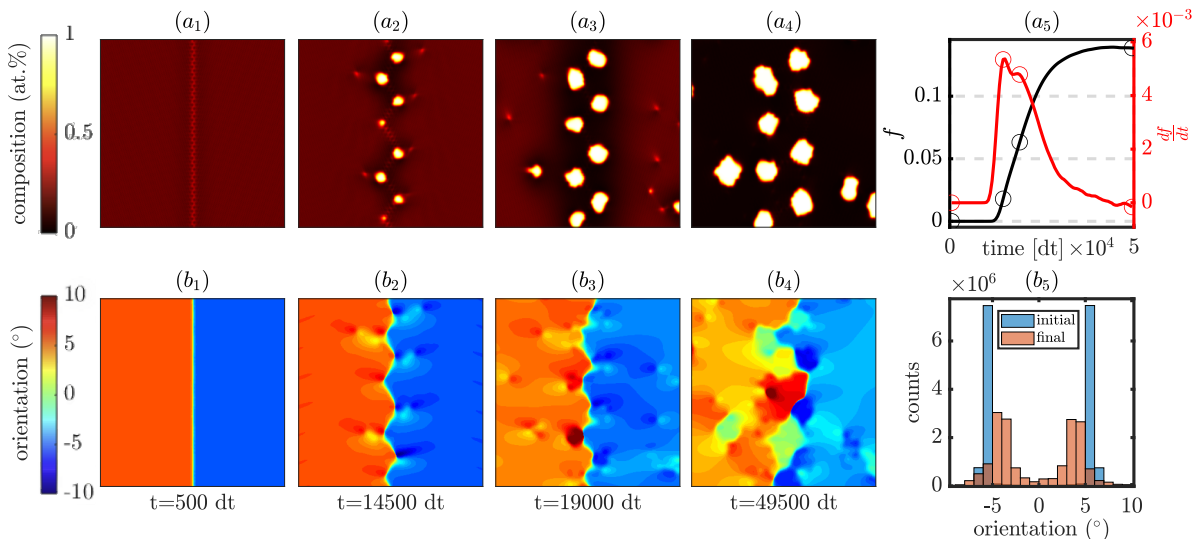


FIG. 2: The sequence of events of a simulation of strain enhanced precipitation. Strain is applied along the y -direction. Panels (a₁)-(a₄) show the evolution of the composition field and panel a₅ shows the associated evolution of the precipitated fraction f as well as df/dt in black and red, respectively, with the values corresponding to panels (a₁)-(a₄) labelled with circles. Panels (b₁)-(b₄) show the behaviour of the local orientation field and (b₅) shows the histogram of orientations of panels (b₁) and (a₄). The first peak in df/dt , corresponding to panels (a₂), b₂ is associated with the precipitation on the buckled interface. The second peak, corresponding to panels a₃, b₃ coincides with precipitate nucleation on dislocations. Panel b₄ shows the late stage coarsening behaviour of the system, which includes the reorientation of A-rich regions close to the grain boundary down to orientations intermediate between zero and the initial orientation of $\pm 6^\circ$.

kept within the range $12.00 \pm 0.05^\circ$. The average density and supersaturation are set to be initially uniform and equal to 0.05 and 0.15, respectively.

The density field is next allowed to relax by setting M_c to zero. This is done so that the amplitude of the density can equilibrate prior to the application of a strain. Then both n and c are subsequently evolved simultaneously by Eqs. 4 and 5, with the application of a biaxial deformation with the tensile direction parallel to the grain boundary.

In order to characterize the behaviour of the system over the course of simulations, three quantities are tracked: The grand potential energy, precipitated fraction f , and local orientation. The grand potential will be used to evaluate the dimensionless system pressure $\bar{P} = P/k_B T^0 \rho^0 V$ as in [28]. The orientation is extracted through local convolutions with oriented density wavelets as in [29]. Finally to calculate the precipitated fraction, local thresholding in composition is applied in conjunction with a Fourier space mask sharply peaked around the dominant wave-vector of the precipitating phase.

We first examine the situation where $\dot{\epsilon} = 0$. While precipitation has been studied with XPFC in the past, to our knowledge no study has been performed with temperature variations in the mobility such as the ones proposed in Eq. (6). We employ the same initial conditions in n and c over a range of values of T and E_A^c and monitor the precipitate fraction, f over the course of dynamical evolution of Eqs. (4) and (5). The fraction f is calculated as described in the previous paragraph, with the compositional filtering chosen at a threshold compositional value of the average of the initial alloy composition and equilibrium B composition values.

Over the course of each isothermal simulation, fluctuations

drive the formation of precipitates along the grain boundary (GB) of the system. A detailed analysis of the geometry, growth rate and nucleation rate of these precipitates is outside of the purview of this paper. Over all temperatures and activation energies examined, the precipitate fraction obeys an Avrami-like behaviour

$$f = f^{eq} \left(1 - e^{-\left(\frac{t}{\tau_{0.5}}\right)^m} \right), \quad (7)$$

where m is an exponent which is determined by the dimensionality and mechanism of the transformation, f^{eq} is the equilibrium precipitate fraction and $\tau_{0.5}$ is a characteristic time-of-the system which is a function of the nucleation and growth-rate. The system pressure was found to exhibit a single dominant peak corresponding to the end of precipitate nucleation. Beyond this time, the system reduces its free energy and pressure through diffusion of solute out of the surrounding supersaturated bulk and into precipitate growth.

Figure 1 shows the isothermal transformation diagram (TTT) curve for a range of model temperatures, demonstrating the inflection about a critical temperature. The scaling of this surface is controlled by the usual driving force for precipitation (competition between bulk and surface energies) as well as the new mobility used here, which also affects the noise strength. At each temperature, the bulk energies are determined through the curvatures of the free energy landscape about the equilibrium wells of Eq. (1) in the space of average density, supersaturation and amplitude of the atomic density field n . The surface energy will be dependent on all of the above along with the effective gradient coefficient of the amplitude arising from the excess energy term, as well as W_c . These parameters are all held fixed for each value of T along

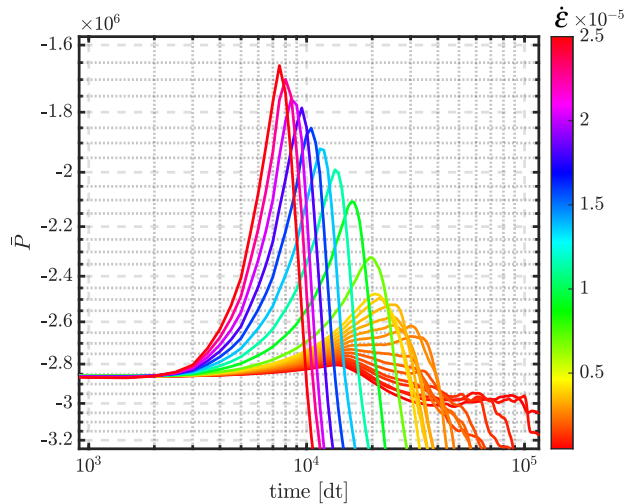


FIG. 3: The system pressure is plotted as a function of system time for different choices of the strain rate. At lower values of $\dot{\epsilon}$ (deep blue), an initial peak followed by oscillations indicating nucleation of dislocations post-precipitation is observed. At larger $\dot{\epsilon}$ (blue–cyan range) a second peak emerges corresponding to a new dislocation assisted precipitation mechanism. At the largest range of $\dot{\epsilon}$ simulated (yellow–red range), a single peak emerges again indicating precipitation assisted through grain boundary buckling.

the curves shown in Figure 1.

We next examine the behaviour of precipitation in the presence of mechanical deformation. We consider a single temperature below with the same initial conditions.

The evolution of a precipitating system under mechanical deformation is shown in Figure 2. At lower values of $\dot{\epsilon}$, f obeys the same qualitative Avrami behavior as the undeformed case. Prior to precipitation, in order to compensate for the applied deformation, the density field undergoes elastic accommodation. The characteristic time-scale, $\tau_{0.5}$, for the precipitation is observed to initially increase with $\dot{\epsilon}$. This occurs due to an accelerated rotation of the bicrystal with increasing $\dot{\epsilon}$, causing a reduction in the effective driving force for precipitation along the boundary. The increase we observe in $\tau_{0.5}$ appears to qualitatively follow a simple $\exp(\gamma^2)$ dependence in the time-scale for precipitation where γ is the bicrystal surface energy’s misorientation dependent component. It is noted that the XPFC model has been shown to reproduce the correct Read-Shockley scaling of solute segregation and grain boundary energy as a function of misorientation in prior studies [30]. We have also performed simulations in the undeformed case with varying orientation that follow this same scaling.

Figure 3 plots the system pressure as a function of time at different strain rates $\dot{\epsilon}$. As in the zero deformation case, at low $\dot{\epsilon}$ the pressure is first found to exhibit a single dominant peak at the initial stages of precipitation, followed by oscillations indicating accommodations by the grain boundary and the formation of any dislocations necessary to support the growth of the population of precipitates.

As strain rate is increased further beyond a critical strain rate of 2×10^{-6} , we observe systematic deviation in the precipitation mechanism. We found three mechanisms that con-

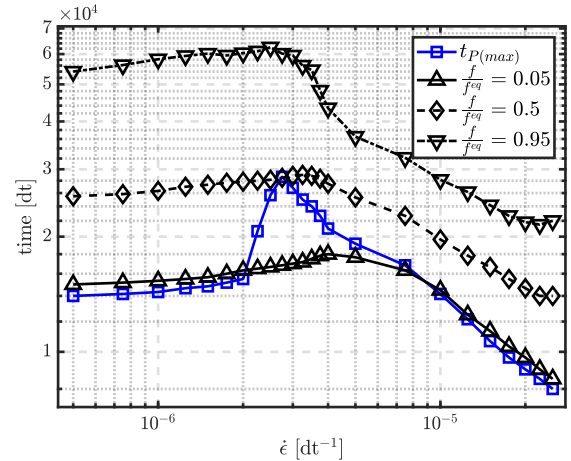


FIG. 4: The times when f/f^{eq} attains 0.05, 0.50 and 0.95 plotted against strain-rate. Also shown in blue is the time at which the system achieves its maximum in pressure $t_{P(max)}$ at each strain-rate. At low $\dot{\epsilon}$, $t_{P(max)}$ corresponds to the initialization of precipitation.

At a critical $\dot{\epsilon} = 2 \times 10^{-6}$, $t_{P(max)}$ diverges significantly from its value during the initiation of precipitation. This occurs because the prominence of the second, plasticity induced, pressure peak surpasses the peak associated with precipitation, as shown in Figure 3. Upon further increase of $\dot{\epsilon}$ beyond 5×10^{-6} , buckling of the GB occurs and $t_{P(max)}$ monotonically decreases past its initial value.

tribute to this deviation, each activating in order of increasing $\dot{\epsilon}$.

At the lower range of $\dot{\epsilon}$, we observe the nucleation of dislocations from initial precipitates or the GB, also shown in Figure 2. It is well known that dislocations act as preferential nucleation sites for precipitation [31]. This has also been examined numerically in prior studies using the XPFC model [22, 23]. If these dislocations nucleate sufficiently quickly, excess solute may diffuse to not only the GB but also towards some dislocations flowing into the bulk of the system. The diffusion of solute towards these dislocations can then induce further precipitation at sites away from the grain boundary. These dislocation nucleation events are characterized by the formation of a new peak in the system pressure that progressively increases in prominence and occurs after initial precipitation along the GB. This peak is subsumed into the pressure shift due to precipitation at intermediate strain rates. This effect is also seen in the data of Figure 3 and Figure 4. The same effect also leads to the emergence of a second peak in df/dt as shown in Figure 5, corresponding to additional precipitate nucleation mechanism. Upon further increase in $\dot{\epsilon}$, the deformation of the system causes the GB to buckle as shown in Figure 2. This buckling further provides preferential sites for precipitate nucleation due to a shifted contact angle as well as curvature induced solute segregation at the cusps. Furthermore, the formation of these precipitates relieves the strain energy stored within these regions. As shown in Figure 3, the resulting pressure for high value of $\dot{\epsilon}$ exhibits only a single prominent peak, which accounts for both a buildup through this buckling mechanism and then a rapid release due to precipitation.

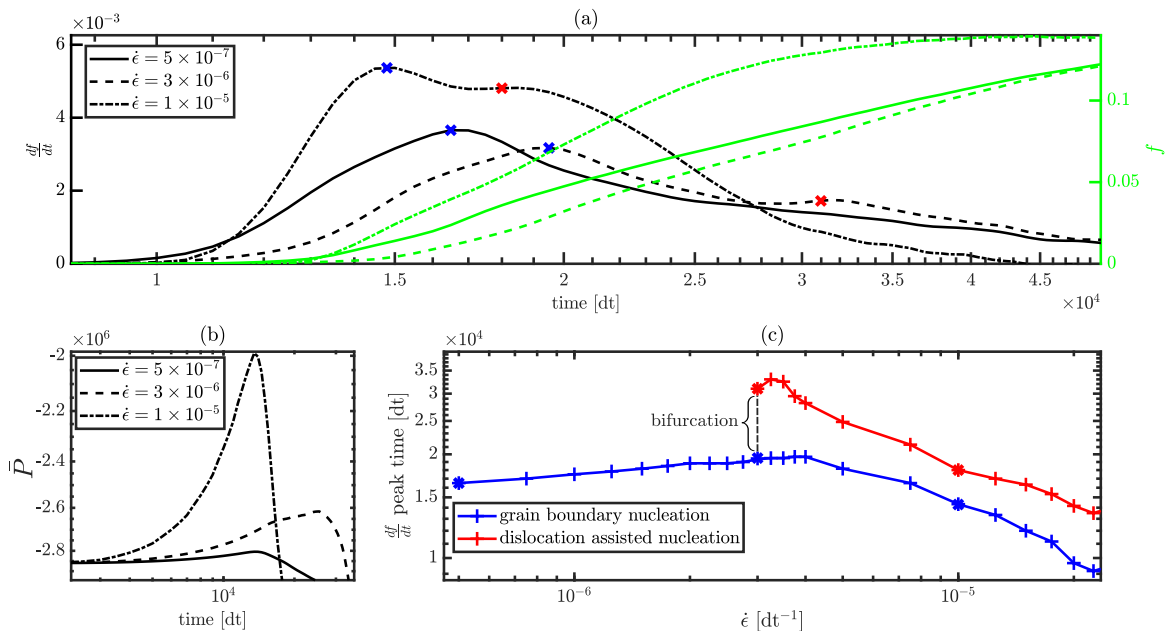


FIG. 5: Panel (a) shows the precipitated fractions (green) and their respective derivatives (black), indicating the first and second peaks (blue and red respectively). The data are plotted for three values of $\dot{\epsilon}$, at progressively higher deformation strain rates. As can be seen the low strain-rate scenario demonstrates a single peak whereas the second and third cases shown here exhibit a prominent second peak in df/dt , associated with dislocation nucleation. Panel (b) shows the corresponding pressure changes associated with these three choices of the strain rate. Panel (c), Blue data show the first peak in the derivative of the precipitated fraction, df/dt versus strain rate. This corresponds to the nucleation of precipitates on the grain boundary. Beyond a critical strain rate of $\dot{\epsilon} = 3 \times 10^{-6} \text{ dt}^{-1}$, the second peak in df/dt appears, shown here in red.

A third mechanism observed at high $\dot{\epsilon}$ deformations is recrystallization at the grain boundary, i.e. the formation of lower-strain A-rich grains. Similar behaviour has recently been modelled in a pure material phase-field crystal model under laser deposition [32]. A typical view of recrystallization events we observe are shown in the orientation field of Figure 2. Due to working in two spatial dimensions these recrystallized regions are not long lived. Indeed, upon performing identical simulations in the scenario where solute is frozen ($M_c, \xi_c = 0$), we see the recrystallized regions initially attain an orientation intermediate to the surrounding bulk grains and eventually coarsen, post nucleation. The mechanism of formation for these recrystallized grains is achieved through collective motion of nucleated dislocations to buckled regions of the grain boundary. In the absence of precipitation, this mechanism has been observed experimentally in the nucleation of twins during continuous deformation of copper bicrystals [33].

To summarize, the collective action of the above three phenomena causes f to exhibit a plateau-like behaviour. As can be seen in Figures 2 and 5, while not halted completely, the maximum in df/dt discontinuously transitions from one to a pair of discrete maxima. Such behaviour in Avrami curves is commonly associated with multiple transformation mechanisms of similar driving forces competing with one another. Our findings have been observed experimentally in the situation when recrystallization is halted by precipitation [34] and in the precipitate fraction of an Al-Zn-Mg-Cu during hot

deformation [3]. It is noted, however, that strain-rate dependence in the present study cannot be quantitatively compared to the mechanisms proposed in [3] as defects cannot frustrate in two dimensions.

It is noteworthy that the three mechanisms described above induce an overall acceleration of the precipitation reaction as it becomes progressively easier to partition the solute in the bulk toward its equilibrium values. As shown in the data of Figure 4, precipitation under large deformation occurs over a shorter time-scale than the case of low (or no) deformation rate below some critical value. These results are also consistent with the typically observed experimental behaviour of TTT diagrams in the presence of deformation [1, 35].

To conclude, we have shown that modified mobilities may be introduced into an improved XPFC alloy model such as those in Eq. (6) to provide a robust atomistic-continuum framework for examination of first order phase transformations in the solid state. We have further shown that upon application of deformation to a bicrystal, beyond an initial stage of elastic compensation where the precipitation largely occurs along a flat grain boundary, new defect assisted nucleation mechanisms begin to compete with classic precipitation mechanisms along the grain boundary. Our results provide an atomistic perspective to the phenomenon of accelerated precipitation commonly observed in deformed systems. We also observe recrystallization events along the grain boundary, which coarsen due to the lack of defect frustration, which is not expected to occur in three dimensions.

ACKNOWLEDGEMENTS

NP thanks The Natural Sciences and Engineering Research Council of Canada (NSERC) and the Canada Research Chairs (CRC) Program for funding support, and the Digital Research Alliance of Canada for computing resources.

* Author to whom correspondence should be addressed. E-mail: alexandre.mamaev@mail.mcgill.ca

- [1] I. Weiss and J. J. Jonas, *Metallurgical Transactions A* **10**, 831 (1979).
- [2] S. Okaguchi and T. Hashimoto, *ISIJ International* **32**, 283 (1992).
- [3] A. Deschamps, F. Bley, F. Livet, D. Fabregue, and L. David, *Philosophical Magazine* **83**, 677 (2003).
- [4] B. Dhakal and S. Swaroop, *Journal of Materials Processing Technology* **282**, 116640 (2020).
- [5] X. Pan, W. He, X. Huang, X. Wang, X. Shi, W. Jia, and L. Zhou, *Surface and Coatings Technology* **405**, 126670 (2021).
- [6] Y. Liao, C. Ye, B.-J. Kim, S. Suslov, E. A. Stach, and G. J. Cheng, *Journal of Applied Physics* **108**, 063518 (2010).
- [7] V. Zhakhovsky, Y. Kolobov, S. Ashitkov, N. Inogamov, I. Nelasov, S. Manokhin, V. Khokhlov, D. Ilnitsky, Y. Petrov, A. Ovchinnikov, *et al.*, arXiv preprint arXiv:2306.09100 (2023).
- [8] M. M. Budzevich, V. V. Zhakhovsky, C. T. White, and I. I. Oleynik, *Phys. Rev. Lett.* **109**, 125505 (2012).
- [9] H. Zurob, Y. Brechet, and G. Purdy, *Acta Materialia* **49**, 4183 (2001).
- [10] Z. Ma, M. Bignon, F. Gao, S. Michalik, and J. Robson, *Journal of Alloys and Compounds* **968**, 172098 (2023).
- [11] K. R. Elder and M. Grant, *Phys. Rev. E* **70**, 051605 (2004).
- [12] K. R. Elder, N. Provatas, J. Berry, P. Stefanovic, and M. Grant, *Phys. Rev. B* **75**, 064107 (2007).
- [13] N. Ofori-Opoku, V. Fallah, M. Greenwood, S. Esmacili, and N. Provatas, *Phys. Rev. B* **87**, 134105 (2013).
- [14] N. Provatas and K. Elder, *Phase-Field Methods in Materials Science and Engineering* (John Wiley & Sons, Ltd, 2010).
- [15] M. Greenwood, N. Provatas, and J. Rottler, *Phys. Rev. Lett.* **105**, 045702 (2010).
- [16] J. Berry, M. Grant, and K. R. Elder, *Phys. Rev. E* **73**, 031609 (2006).
- [17] J. Berry, N. Provatas, J. Rottler, and C. W. Sinclair, *Phys. Rev. B* **89**, 214117 (2014).
- [18] D. Burns, N. Provatas, and M. Grant, *Acta Materialia* **267**, 119712 (2024).
- [19] P. Stefanovic, M. Haataja, and N. Provatas, *Phys. Rev. Lett.* **96**, 225504 (2006).
- [20] P. Stefanovic, M. Haataja, and N. Provatas, *Phys. Rev. E* **80**, 046107 (2009).
- [21] D. Burns, N. Provatas, and M. Grant, *Modelling Simul. Mater. Sci. Eng.* **30**, 064001 (2022).
- [22] V. Fallah, J. Stolle, N. Ofori-Opoku, S. Esmacili, and N. Provatas, *Phys. Rev. B* **86**, 134112 (2012).
- [23] V. Fallah, N. Ofori-Opoku, J. Stolle, N. Provatas, and S. Esmacili, *Acta Materialia* **61**, 3653 (2013).
- [24] C. Wei, S. Tang, Y. Kong, X. Shuai, H. Mao, and Y. Du, *Materials* **16**, 10.3390/ma16051841 (2023).
- [25] B. A. Jugdutt, N. Ofori-Opoku, and N. Provatas, *Phys. Rev. E* **92**, 042405 (2015).
- [26] M. J. Frick, N. Ofori-Opoku, and N. Provatas, *Phys. Rev. Mater.* **4**, 083404 (2020).
- [27] J. Mellenthin, A. Karma, and M. Plapp, *Phys. Rev. B* **78**, 184110 (2008).
- [28] G. Kocher and N. Provatas, *Phys. Rev. Lett.* **114**, 155501 (2015).
- [29] Z. Wang, J. Li, Y. Guo, S. Tang, and J. Wang, *Computer Physics Communications* **184**, 2489 (2013).
- [30] J. Stolle and N. Provatas, *Computational Materials Science* **81**, 493 (2014).
- [31] J. W. Cahn, *Acta Metallurgica* **5**, 169 (1957).
- [32] D. Burns, N. Provatas, and M. Grant, *Structural Dynamics* **11**, 014101 (2024).
- [33] H. Miura, T. Sakai, R. Mogawa, and G. Gottstein, *Scripta Materialia* **51**, 671 (2004).
- [34] S. F. Medina, *Journal of Materials Science* **32**, 1487 (1997).
- [35] S. Chen, L. Li, Z. Peng, X. Huo, and J. Gao, *Journal of Materials Research and Technology* **9**, 15759 (2020).

Supplemental Material

1 Free energy

The functional form of the free energy we employ is presented in the main body of the letter. It is repeated below for convenience:

$$\frac{\Delta F}{k_B T^0 \rho^0} = \tau \int d\mathbf{r} \left\{ \frac{1}{2} n^2 - \frac{\eta}{6} n^3 + \frac{\chi}{12} n^4 + \omega \Delta F_{mix} + \frac{W_c}{2} |\nabla c|^2 - \frac{1}{2} n \int d\mathbf{r}' C_{nm}^{(2)}(|\mathbf{r} - \mathbf{r}'|) n' \right\}, \quad (1a)$$

$$\Delta F_{mix} = (1 + n) \left\{ c \log\left(\frac{c}{c_0}\right) + (1 - c) \log\left(\frac{1 - c}{1 - c_0}\right) \right\}. \quad (1b)$$

The free energy and correlation function parameters we employ that fully specify our particular material of interest are shown in Table 1. These are held fixed over the course of every simulation we perform. The respective phase diagram corresponding to these parameters is also shown in Figure 1. Phase diagram construction is performed by numerically identifying common tangents in the free energy landscape after an assumed mode expansion for the density is inserted into the free energy and a subsequent minimization of the mode expansion amplitudes is performed as described in cf. [?, ?].

c_0	η	χ	ω	W_c	k_A	k_B	T_A^0	T_B^0	$\sigma_{A,0}$	$\sigma_{B,0}$	$\sigma_{A,1}$	$\sigma_{B,1}$	$A_{A,0}$	$A_{B,0}$
0.5	1.4	1	0.005	0.25	2π	2.27π	100	100	2.5	2.84	1.4	1.4	0.75	0.75

Table 1: Free energy parameters for all choices of temperature, strain-rate and supersaturation. Eqs. 1a and 1b

2 Discretization and dynamics

Dynamical evolution of density and composition fields was performed with a semi-implicit Fourier spectral method [?]. The numerical values of the parameters employed in these simulations are shown in Table 2. These choices were made to allow for simultaneous precipitation and plastic response for the strain-rates we employ. The choice of strain-rate was set such that a non-negligible amount of strain-energy could be imparted into the system prior to precipitation, and the total strain imparted stayed within the realm of experimentally achievable deformation.

Each choice of temperature, strain-rate and activation energy were simulated using the same discretization scheme. We employ a two-dimensional system box of $N_x \times N_y$ pixels with a discretization of dx and dy along each respective axis. Time was discretized with

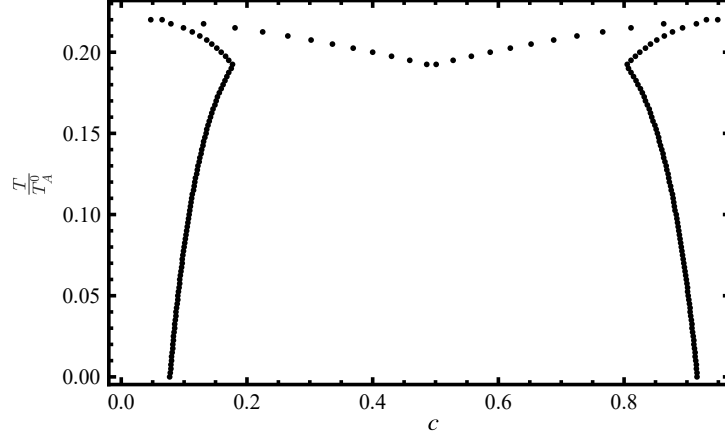


Figure 1: Phase diagram associated with free energy parameters shown in Table 1 with respect to dimensionless temperature, T/T^0 and concentration c . The average density is fixed here at 0.05 which is sufficiently distant from any phases outside of the liquid and solid phase.

an increment dt . The parameters we employ for our simulations are shown in Table 2. The spatial discretizations along each axis are varied along with the initial grain boundary misorientation to allow for an integer number of atoms initially present along both axes inside the simulation box. These variations are kept within the ranges of $12.00^\circ \pm 0.05^\circ$ and 0.10 ± 0.01 for the misorientation and spatial discretization respectively. We do not observe significant deviations in the behaviour precipitated fraction or the pressure over different parameter choices within our set tolerance (solutions are typically not unique within the tolerance range).

M_n^0	M_c^0	E_A^c	E_A^n	β	N_n	N_c	N_x	N_y	dx	dy	dt
0.02	1	0.1-1	10	0.1	0.05	0.01	4096	4096	0.10 ± 0.01	0.10 ± 0.01	0.5

Table 2: Parameters employed for numerical simulation of dynamical evolution of n and c fields. The discretizations along the x and y axes along with the initial grain boundary misorientation vary slightly between simulations to accommodate an integer number of lattice sites depending on the initial supersaturation imposed.